Journal of Hazardous Materials 463 (2024) 132898

Contents lists available at ScienceDirect

Journal of Hazardous Materials

journal homepage: www.elsevier.com/locate/jhazmat

Research Paper

Synchronous fluorescence detection of nitrite in meat products based on dual-emitting dye@MOF and its portable hydrogel test kit

Siyang Deng [a,d], Junmei Liu [a,d], Dong Han [a], Xinting Yang [b,c], Huan Liu [b,c,*], Chunhui Zhang [a,**], Christophe Blecker [d]

[a] Key Laboratory of Agro-Products Processing, Ministry of Agriculture and Rural Affairs, Institute of Food Science and Technology, Chinese Academy of Agricultural Sciences, Beijing 100193, China
[b] Research Center for Information Technology, Beijing Academy of Agricultural and Forestry Sciences, Beijing 100097, China
[c] National Engineering Research Center for Information Technology in Agriculture, Beijing 100097, China
[d] University of Liège, Gembloux Agro-Bio Tech, Unit of Food Science and Formulation, Passage des Déportés 2, Gembloux B-5030, Belgium

HIGHLIGHTS

- A ratiometric fluorescent sensor for NO_2^- using Rh6G@UIO-66-NH_2 was displayed.
- Synchronous fluorescence spectroscopy provides essential information for sensor.
- A rapid-responsive LMOF-gelatin-based portable kit was put forward to detect NO_2^-.
- This portable kit can detect NO_2^- in both colorimetric and fluorescence modes.

GRAPHICAL ABSTRACT

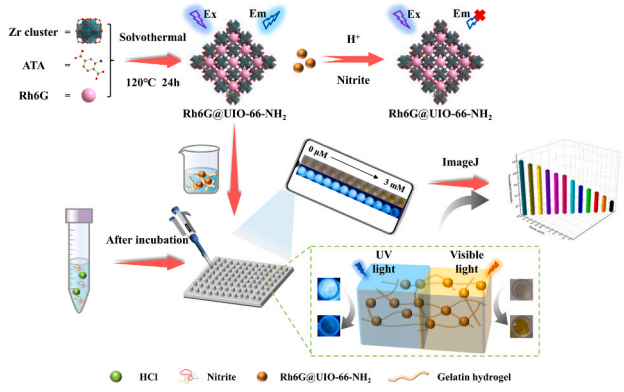

ARTICLE INFO

Editor: Lingxin CHEN

Keywords:
NO_2^-
Rh6G@UIO-66-NH_2
Luminescent metal organic framework
Dual-mode detection
On-spot visualization

ABSTRACT

A novel ratiometric fluorescent nanoprobe (Rh6G@UIO-66-NH_2) was fabricated for efficient nitrite (NO_2^-) detection in the present study. When NO_2^- was introduced, it interacted with the amino groups on the surface of Rh6G@UIO-66-NH_2, forming diazonium salts that led to the quenching of blue fluorescence. With this strategy, a good linear relationship between NO_2^- concentration and the fluorescent intensity ratio of the nanoprobe in the range of 1–100 μM was established, with a detection limit of 0.021 μM. This dual-readout nanosensor was applied to analyze the concentration of NO_2^- in real meat samples, achieving satisfactory recovery rates of 94.72–104.52%, highlighting the practical potential of this method. Furthermore, a portable Gel/Rh6G@UIO-66-NH_2 hydrogel test kit was constructed for on-spot dual-mode detection of NO_2^-. This kit allows for convenient colorimetric analysis and fluorometric detection when used in conjunction with a smartphone. All the photos taken with the portable kit was converted into digital information using ImageJ software. It provides colorimetric

* Corresponding author at: Research Center for Information Technology, Beijing Academy of Agricultural and Forestry Sciences, Beijing 100097, China.
** Corresponding author.
E-mail addresses: liuhuan@nercita.org.cn (H. Liu), dr_zch@163.com (C. Zhang).

https://doi.org/10.1016/j.jhazmat.2023.132898
Received 4 September 2023; Received in revised form 7 October 2023; Accepted 29 October 2023
Available online 31 October 2023

and fluorescent visual detection of NO_2^- over a range of 0.1–1.5 mM, achieving a direct quantitative tool for NO_2^- identification. This methodology presents a promising strategy for NO_2^- detection and expands the application prospects for on-spot monitoring of food safety assessment.

1. Introduction

Nitrite (NO_2^-) has been used as an essential additive in processed meat products during the curing stage for centuries. It's valued for its ability to provide excellent color protection, act as an antioxidant, enhance flavor, and served as an antiseptic agent [1–3]. Serving as a color retention agent, NO_2^- plays a pivotal role in producing rose-colored nitrosyl myoglobin by reacting with myoglobin, thereby enhancing the visual appeal of meat products [4]. Additionally, due to its antiseptic and antioxidation properties, NO_2^- is used to extend the shelf life of meat products and inhibit the growth of pathogenic and putrefying bacteria (particularly *Clostridium botulinum*), thereby enhancing the safety of meat products [5–7]. Nevertheless, it is worth noting that excessive consumption of NO_2^- can cause several adverse health effects, including methemoglobinemia, esophageal and gastric cancers, and so on [8–10]. While NO_2^- itself is not a carcinogen, it can degrade to nitric oxide inside the meat system, which can react with secondary amines to form carcinogenic and mutagenic N-nitrosamines in the stomach [11,12]. It is worth noting that NO_2^- has been classified as a carcinogen listed by the World Health Organization (WHO) and is subject to restrictions by worldwide authorities [13]. Therefore, it is of vital significance to accurately detect NO_2^- content in food systems.

Several classic NO_2^- detection techniques, such as electrochemistry, chromatography, and spectrophotometry, have been published to date [14–16]. However, these traditional analysis methods have their limitations, including the need for sophisticated and costly equipment, the requirement for professional and trained operators, and high testing costs. In contrast, fluorescence detection methods relying on metal organic frameworks (MOFs) are preferred for NO_2^- assays due to their simplicity, sensitivity, accuracy, and cost-effectiveness. MOFs are well-known for their representative and adjustable three-dimensional (3-D) network structure, appropriate specific areas, and highly uniform nanoscale cavities, which effectively enhance targets concentration and promote recognition and sensitivity of guest targets [17]. As a subcategory of MOFs, dye@MOF, which consists of fluorescent dye molecules and fundamental MOF architecture, has gained prominence as a candidate for fluorescent sensing applications [18]. Dye@MOF can provide different responses and amplify emission ranges for targets based on the dual-emitting or multi-emitting fluorescence intensities of luminescent guest species and MOF [19]. Up until now, most reported MOFs-based nanoprobes have focused on single-emission sensors for NO_2^- detection. However, single-emission sensors may be susceptible to non-detection factors or environmental interference during the detection process [17,20,21]. Hence, it is of significance to propose an efficient dye@MOF sensing platform to enhance accuracy and anti-interference based on ratiometric fluorescence.

As far as we know, synchronous fluorescence spectroscopy (SFS) can simultaneously scan excitation and emission wavelengths, and the corresponding SFS spectrum is obtained on the condition of maintaining a certain wavelength difference ($\Delta\lambda = \lambda em - \lambda ex$). Given that distinct fluorophores possess intrinsic λex and λem, the collection of SFS provides a direct means of performing multicomponent analysis on complex systems by scanning multiple wavelengths. Therefore, it has proven to be a highly effective method for revealing the comprehensive chemical properties of samples [22,23]. The outstanding advantages of SFS are that it can simplify spectra, reduce scattering light interferences and spectral overlap, and enhance selectivity to a large extent, compared to standard fluorescence spectroscopic methods [24,25]. Therefore, the SFS spectrum holds great potential for simultaneously providing information about MOF and luminescent dye molecules when applied to the analysis of NO_2^- in a food matrix.

It is well known that the 3-D framework structure of numerous MOFs is vulnerable to collapse when exposed to hydrophilic media for a long period of time. However, previous studies have proved that the remarkable stability of UIO-66-NH_2 in an aqueous solution, including acidic solutions, as well as at high temperatures. This stability makes it particularly suitable for applications as sensors with the state of tiny particles or powders in sensing systems [26,27]. To enhance practicality and convenience in applications, one of the ideal strategies is the creation of a cast and straightforward MOF thin film containing the as-synthesized dye@UIO-66-NH_2 powder and hydrogel. This approach can facilitate the efficient development of MOF-based composites. Hydrogel is currently recognized as a highly hydrophilic polymer chain with 3-D solid networks, facilitating the dispersion of MOF powders within it [28,29]. In addition, this waterproof dye@MOF with high activity can also tune the properties of hydrogel as a reinforcing additive [30]. Hydrogel is useful for detecting various targets in a variety of sensing applications, particularly in the development of visual detection platforms due to its minimal fluorescence emission and background color [31].

In response to the above-mentioned circumstance, this study establishes a novel fluorescent sensing nanoprobe based on fluorescein (Rh6G) and Zr-based MOF (UiO-66-NH_2), donated as Rh6G@UiO-66-NH_2. This was achieved by in situ encapsulating Rh6G molecules into the Zr-MOF architecture through solvothermal conditions (Scheme 1A). As expected, the synthesized Rh6G@UiO-66-NH_2 nanocomposite displays the dual emission characteristics due to energy transfer from Zr-based MOF to organic dye. Therefore, the SFS technique, coupled with the dye@MOF, was applied for the rapid detection of NO_2^- residues in meat product. As a self-calibrating fluorescence sensor, Rh6G@UiO-66-NH_2 can accurately, sensitively, and selectively detect NO_2^- by using the ratio of the fluorescence intensity I_{Rh6G}/I_{MOF}, which shows a clearly linear relationship with different concentrations of NO_2^-. More significantly, an available sensing platform was fabricated through immobilizing Rh6G@UiO-66-NH_2 on a gelatin hydrogel matrix, through which semi-quantitative detection of NO_2^- can be achieved by the naked eye based on fluorescent color under ultraviolet (UV) light. Accordingly, this study offered significant MOF nanocomposite and immobilized hydrogels for the quantification and visualization of NO_2^- residues in meat products.

2. Materials and methods

2.1. Chemicals and materials

Chemicals were procured from commercial sources. Zirconium chloride ($ZrCl_4$), 2-amino-terephthalic acid (ATA), N, N-dimethylformamide (DMF), acetic acid (AA), hydrochloric acid (HCl), potassium ferrocyanide, zinc acetate, and rhodamine 6 G (Rh6G) were obtained from Aladdin reagent company (Shanghai, China). NO_2^- and aqueous solutions containing interference ions (NO_3^-, SO_4^{2-}, CO_3^{2-}, Cl^-, K^+, Na^+, Ca^{2+}, Mg^{2+}, Pb^{2+}, Zn^{2+}, Cu^{2+}, Mn^{2+}, Fe^{2+}, Fe^{3+}, Al^{3+}, $H_2PO_4^-$ and HPO_4^{2-}) were sourced from Macklin Biochemical Co., Ltd. (Shanghai, China). All reagents and solvents were commercially available and used as received, without undergoing purification procedure.

2.2. Synthesis of UiO-66-NH_2

UiO-66-NH_2 was synthesized using a solvothermal method based on a previously reported approach with minor modifications [32]. In

summary, $ZrCl_4$ (0.5 mmol/L) and ATA (0.5 mmol/L) were dissolved in DMF (50 mL) at room temperature, and the resulting mixture underwent ultrasonic treatment for 20 min. Subsequently, 5 mL of acetic acid was added to the obtained solution, followed by an additional 10 min of sonication. The resulting mixture was then transferred to a 100 mL Teflon reactor and maintained at 120 °C for 24 h. After cooling to room temperature, the faint yellow powder obtained was centrifuged, washed with DMF and methanol (each wash repeated at least three times) to remove any remaining unreacted ligands and metals, and finally dried under vacuum at 120 °C for 12 h.

2.3. Synthesis of Rh6G@UiO-66-NH_2

According to the reported literature [33], UiO-66-NH_2 (100 mg) was dispersed in ethanol (20 mL) containing varying Rh6G concentrations (0, 0.5, 1.0, 1.5, and 2.0 mmol/L). Afterward, the mixture was transferred into a Teflon reactor (100 mL) after being ultrasonically treated for 5 min and heated at 120 °C for 24 h. Then, the resulting precipitates were centrifuged and washed multiple times with ethanol and ultrapure water until the supernatant became colorless, effectively removing excess Rh6G dye. The Rh6G@UIO-66-NH_2 powders were collected and dried in a vacuum at 120 °C for 12 h.

2.4. General procedure of nitrite determination using Rh6G@UIO-66-NH_2 sensor

To investigate the sensing system's response to NO_2^-, a series of aqueous solutions with different NO_2^- concentrations (ranging from 0 to 3 mM) were prepared and tested them in an acidic environment at room temperature. To generate an initial Rh6G@UIO-66-NH_2 suspension, 5.0 mg of synthesized Rh6G@UIO-66-NH_2 powder was added to 20 mL of deionized water and stirred the mixture magnetically for 20 min. The resulting Rh6G@UIO-66-NH_2 stock suspension was stored in a refrigerator at 4 °C for further use. Next, 100 μL of Rh6G@UIO-66-NH_2 stock solution was mixed with 800 μL of HCl solution (0.05 M), and 100 μL different concentrations of a freshly prepared NO_2^- aqueous solution was incrementally added to the above mixture. The resulting mixed solution was thoroughly incubated at room temperature for 15 min, the reacted solution was transferred into a fluorescent cuvette before recording the synchronous fluorescence spectra with $\Delta\lambda = 60$ nm. In addition, each peak was measured more than three times, with the average values utilized to calculate the intensity ratio.

2.5. Selectivity and anti-interference test using Rh6G@UIO-66-NH_2 sensor

To examine the selectivity and anti-interference capability of the Rh6G@UIO-66-NH_2 probe for NO_2^-, the fluorescent spectra of the mixture of the Rh6G@UIO-66-NH_2 and the interfering ions were investigated in the absence and presence of NO_2^-. Various anions and cations that coexist with NO_2^- in meat products (such as NO_3^-, SO_4^{2-}, CO_3^{2-}, Cl^-, K^+, Na^+, Ca^{2+}, Mg^{2+}, Pb^{2+}, Zn^{2+}, Cu^{2+}, Mn^{2+}, Fe^{2+}, Fe^{3+}, Al^{3+}, $H_2PO_4^-$, and HPO_4^{2-}) were introduced into the detection system as interference, replacing or coexisting with the NO_2^- standard solution. Briefly, the procedure involved mixing 100 μL of the selected ion (1 mM) with 100 μL of the Rh6G@UIO-66-NH_2 suspension (0.25 mg/ mL) in a test tube. The mixture was then combined with 800 μL of a 0.05 M HCl solution and allowed to react at room temperature for 15 min. Simultaneously, an identical solution described above was prepared, followed by the sequential addition of 100 μL of NO_2^- (100 μM) into the test tube, again allowing it to react for 15 min at room temperature. Subsequently, all prepared solutions were transferred to a quartz cuvette for recording fluorescence spectra. And the fluorescence intensity was recorded three times to ensure the stability and reliability of the experimental results.

2.6. Analysis of real samples using Rh6G@UIO-66-NH_2 sensor

Five representative categories of commercial meat products, including pork, beef, and chicken, were purchased from a local supermarket (Beijing, China). All meat samples were collected to verify the feasibility of the self-calibration fluorescence sensor, and specific information about each sample is provided in Table S1. It is worth mentioning that the NO_2^- was processed and extracted from meat product samples in accordance with the China national standard (GB

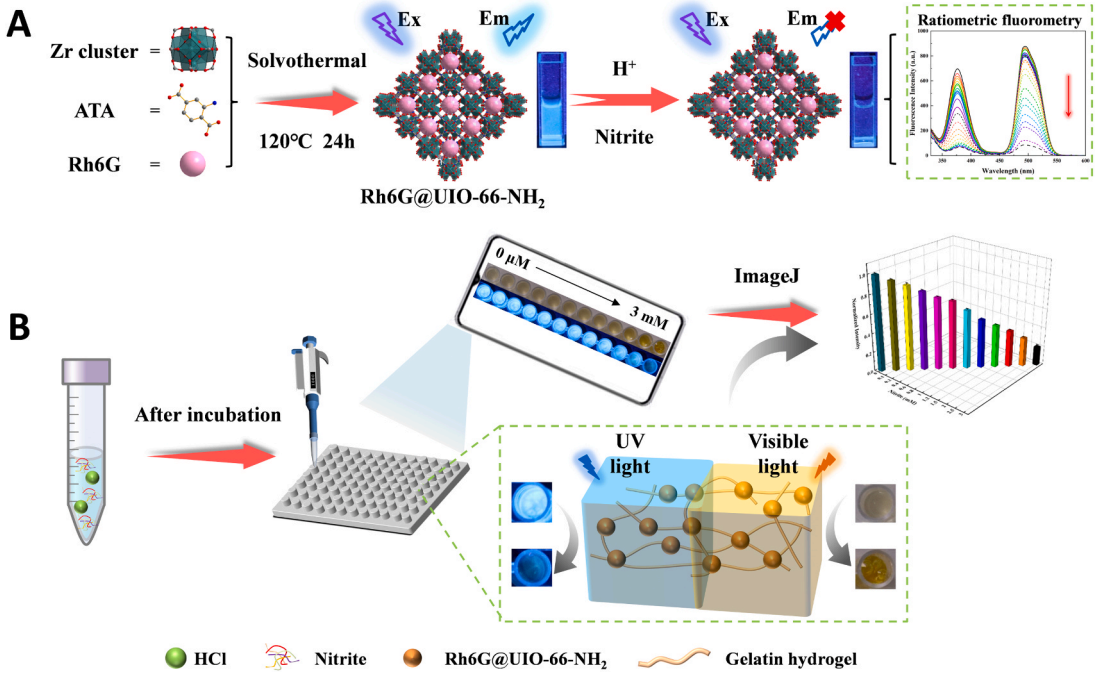

Scheme 1. (A) Schematic illustration of the synthetic procedure for the luminescent metal organic framework (LMOF) Rh6G@UIO-66-NH_2 and its sensing machanism toward analytes of NO_2^-. (B) Reaction process of the Gel/ Rh6G@UIO-66-NH_2 hydrogel test kit for NO_2^- assay.

5009.33–2016). And the detailed extraction procedure was referred to our previous report [34]. In brief, 5.0 g of each of the following: sausage, bacon, ham, stewed beef, and braised chicken, were weighed and placed into separate 250 mL glass conical flask with stoppers. To each flask, 12.5 mL of saturated borax solution (50 g/L) and approximately 150 mL of distilled water at 70 °C were added. The conical flasks were then heated in a boiling water bath for 15 min before being cooled to room temperature. To transfer the extracted liquid, 5 mL of potassium ferrocyanide (106 g/L), 5 mL of zinc acetate (220 g/L), and distilled water were added sequentially, followed by thorough shaking. The resulting homogenate was left to stand for 30 min and then filtered using filter paper to remove insoluble and unwanted substances. Finally, 30 mL of the initial filtrate was discarded, and the remaining filtrate was preserved in a refrigerator at 4 °C for future use. The real meat product samples were used to measure NO_2^- by the fluorescence sensor Rh6G@UIO-66-NH_2, the same procedures and conditions were followed as 2.4. However, the pure NO_2^- solution was replaced by an equal volume of meat product extraction spiked with different concentrations of NO_2^-.

2.7. Preparation of portable test kit using Rh6G@UiO-66-NH_2 immobilized gelatin hydrogels

Generally, 1.0 g of gelatin powder was dissolved in 9 mL of deionized water at 60 °C, and then 10 mL of Rh6G@UiO-66-NH_2 suspension (0.5 mg/mL) was added to the above solution. The mixture was subsequently cooled to 40 °C and stirred thoroughly to ensure uniformity. Then, 150 μL of the prepared solution was carefully transferred into a 96-well microplate to form the gelatin hydrogel. The hydrogel was then stored at room temperature (25 °C) for future use.

2.8. Nitrite determination using Gel/Rh6G@UiO-66-NH_2 hydrogel test kit

For detecting NO_2^-, 800 μL of HCl solution (0.05 mol/L) and 100 μL of different concentrations of NO_2^- solution were mixed together, and then 150 μL of the above reaction solution was introduced to the gelatin hydrogel kit for incubation for 30 min. Then, the color change of the gelatin hydrogel was captured using a smartphone camera. To ensure the stability of the light source during image capture, white light bulbs were incorporated to simulate visible light, along with a 365 nm UV lamp for simulating UV light in the darkroom. And a fixed angle and position was selected for image capture to maximize image quality and minimize background interference. Under the predetermined illumination of visible and ultraviolet lights, the color of the Gel/Rh6G@UiO-66-NH_2 test kit was captured using a smartphone, and then the images were analyzed by ImageJ software. All measurements were conducted in triplicate.

2.9. Selectivity and anti-interference using Gel/Rh6G@UiO-66-NH_2 hydrogel test kit

The selectivity and anti-interference capability of the Gel/Rh6G@UIO-66-NH_2 test kit for NO_2^- were investigated by introducing the same interfering ions that has been discussed in Section 2.5. These ions were introduced both in the absence and presence of NO_2^- into the Gel/Rh6G@UIO-66-NH_2 test kit. To carry out the experiment, a mixture of 800 μL of HCl solution (0.05 mol/L) and 100 μL of the selected ion (1 mM) solution were prepared. Simultaneously, an identical solution described above was prepared, and then 100 μL of NO_2^- (100 μM) was sequentially added into the test tube. Then, 150 μL of the resulting reaction solution was introduced to the Gel/Rh6G@UIO-66-NH_2 hydrogel test kit and incubated for 30 min at room temperature. All test kit images were captured under visible and ultraviolet light irradiation, and the color information in these images was analyzed using a smartphone. All measurements were performed in triplicate.

2.10. Apparatus

Both 3-D fluorescence spectra and synchronous fluorescence spectra were collected using a Hitachi F-7000 fluorescence spectrophotometer (Tokyo, Japan). The acquisition parameters for 3-D fluorescence spectroscopy were as follows: The excitation wavelength range was changed from 200 nm to 600 nm, and emission wavelength was changed from 200 nm to 700 nm in steps of 5 nm, respectively. The slit width of excitation and emission was set to 5 nm. The scanning rate and detector voltage were 30,000 nm/min and 500 V, respectively. For synchronous fluorescence spectra, excitation and emission were collected simultaneously, with the photoexcitation wavelength (λEx) ranging from 200 nm to 600 nm in 1 nm increments. The wavelength offsets ($\Delta\lambda = \lambda Em - \lambda Ex$) was set at 60 nm. Slit widths for both excitation and emission were maintained at 5 nm. The scan speed was set at 1200 nm/min, and the PMT detector voltage (V) was adjusted to medium (700 V). To ensure accuracy and minimize measurement errors, fluorescence measurements were conducted in triplicate for each sample, and subsequent analysis used the average of these three measurements. UV–vis spectra were recorded by a UV 3600i Plus spectrophotometer (Shimadzu, Japan). For powder X-ray diffraction (PXRD) patterns, measurements were conducted using the Panalytical X-ray Diffractometer Smartlab-9 kW (Tokyo, Japan) with Cu Kα radiation ($\lambda = 1.5406$ Å, 40 kV, 250 mA). Fourier transform infrared (FTIR) spectra were obtained within the 4000–400 cm^{-1} region using a Thermo Scientific Nicolet IS5 FTIR spectrophotometer. Scanning electron microscopy (SEM) images were captured using the FEI Inspect F50 scanning electron microscope. Physical adsorption property measurement was carried out using a porosity analyzer Autosorb-iQ2-MP (Quantachrome, USA) with N_2 adsorption analysis.

3. Results and discussion

3.1. Characterizations of Rh6G@UIO-66-NH_2

The crystal structures of both the as-prepared UiO-66-NH_2 and Rh6G@UiO-66-NH_2 were characterized based on the PXRD patterns (Fig. 1 A). The characteristic peaks of the synthesized UiO-66-NH_2 at 2θ angles of 7.30 °, 8.42 °, and 25.62 ° closely matched well with the simulated ones [35], confirming the successful synthesis and high crystallinity of the desired sample. Upon adsorption of different concentrations of fluorescein Rh6G, these analogous PXRD patterns showed little change in the crystalline framework (Fig. 1B). Simultaneously, no characteristic diffraction peaks of Rh6G were observed in Rh6G@UiO-66-NH_2, demonstrating that the absorption of Rh6G presumably had a negligible effect on the UiO-66-NH_2 lattice. Rh6G appeared to be encapsulated or embedded into the cavity rather than physically aggregating on the surface of the UiO-66-NH_2 crystal due to the favorable dispersion of Rh6G and the unique porous framework of the MOF [33]. Afterward, FTIR spectra of UiO-66-NH_2 and Rh6G@UiO-66-NH_2 were recorded to characterize their molecular structure, as shown in Fig. 1C and D. In the UiO-66-NH_2 spectra (Fig. 1C), two characteristic peaks at 483 cm^{-1} and 665 cm^{-1} were assigned to the O–H and C–H vibrations of UiO-66-NH_2, and a peak at 770 cm^{-1} corresponded to the stretching vibration of Zr–O bonds. Additionally, peaks at 1387 cm^{-1}, 1571 cm^{-1} and 1655 cm^{-1} were assigned to the C═O stretching vibration of the carboxyl group, and the peaks at 3365 and 3431 cm^{-1} corresponded to the symmetric and asymmetric N–H vibrations of the amino group from the organic ligand ATA [36,37]. Similar results were observed in the Rh6G@UiO-66-NH_2 spectra, except for the appearance of the C═O stretching vibration peak at 1655 cm^{-1}, which was attributed to anchored Rh6G molecules on UiO-66-NH_2. Moreover, no distinctive peaks corresponding to Rh6G were detected in the Rh6G@UiO-66-NH_2 nanomaterial, indicating that the majority of Rh6G molecules were encapsulated within the pores of UiO-66-NH_2, with their vibrations of Rh6G impeded by the 3-D structure

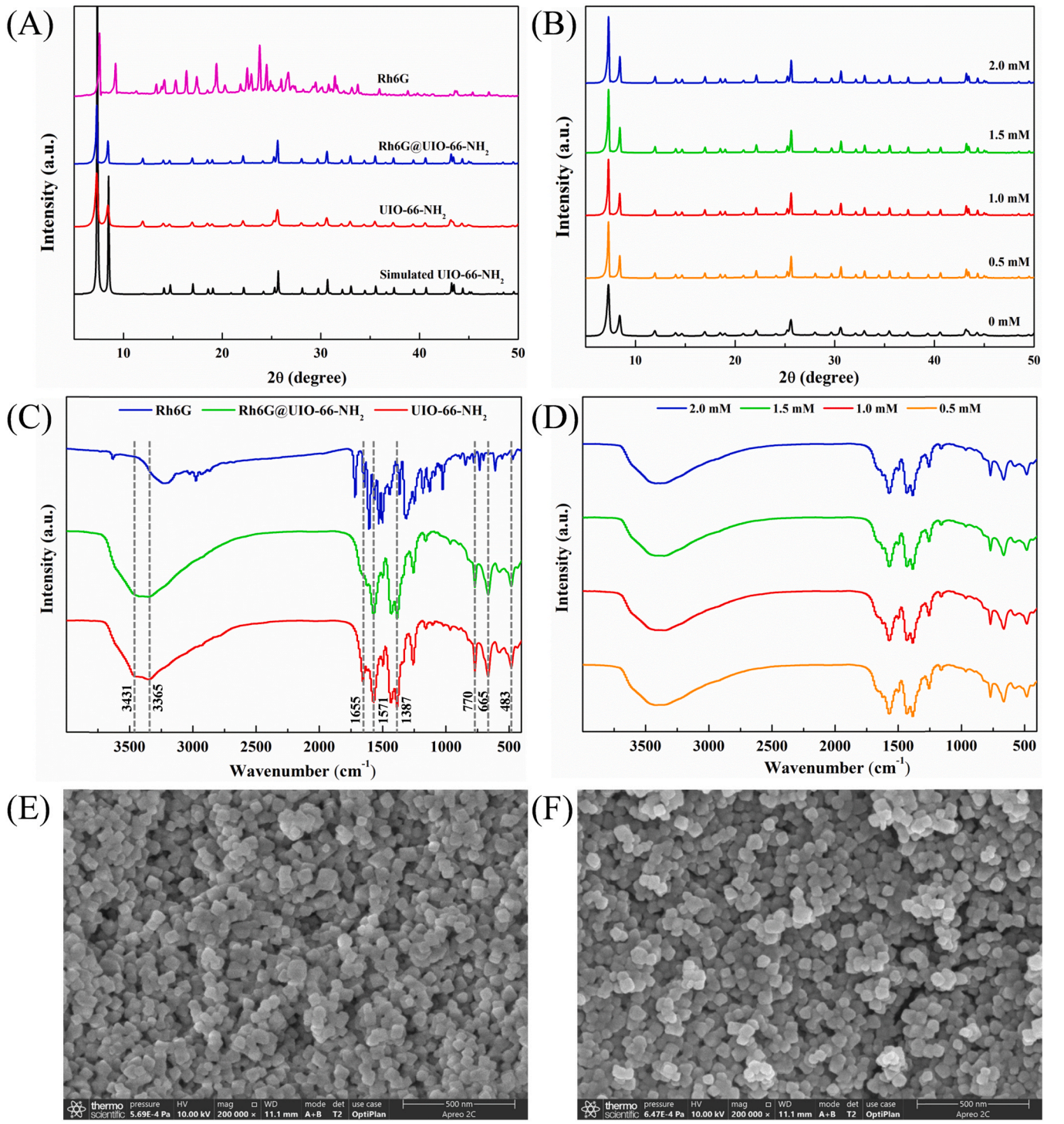

Fig. 1. (A) The PXRD patterns for the simulated UIO-66-NH_2 (black curve), UIO-66-NH_2 (red curve), Rh6G@UIO-66-NH_2 (blue curve), and Rh6G (pink curve). (B) The PXRD patterns of Rh6G@UIO-66-NH_2 nanoparticles with different Rh6G concentrations. (C) The FT-IR patterns of UIO-66-NH_2 (red curve), Rh6G@UIO-66-NH_2 (green curve), and Rh6G (blue curve). (D) The FI-TR patterns of Rh6G@UIO-66-NH_2 nanoparticles with different Rh6G concentrations. SEM images of synthesized (E) UIO-66-NH_2 and (F) Rh6G@UIO-66-NH_2.

of UiO-66-NH_2 [38]. There was no visible difference in FT-IR spectra among Rh6G@UiO-66-NH_2 samples with different concentrations, further indicating the minimal influence of the organic dye on the crystal structure of UiO-66-NH_2. The morphological and structural characterizations of UiO-66-NH_2 and Rh6G@UiO-66-NH_2 were illustrated through SEM images. In Fig. 1E and 1F, both UiO-66-NH_2 and Rh6G@UiO-66-NH_2 nanomaterials exhibited irregular octahedral particles, each approximately 75 nm in size, with no apparent differences in morphology observed before and after Rh6G encapsulation. Comparing the porosity of UIO-66-NH_2 before and after encapsulating fluorescein Rh6G can help verify their permanent porosities and functionalization. The nitrogen (N_2) absorption-desorption isotherms of UIO-66-NH_2 and synthesized Rh6G@UIO-66-NH_2 were recorded at 77 K, and the results of porosity analysis and surface area are presented in Fig. S1. The adsorption isotherms clearly exhibited a sharp increase in N_2 adsorption at very low relative pressures, followed by a gradual rise up to high

relative pressures, while a small hysteresis observed at relatively high pressures. Consequently, it can be deduced that both UIO-66-NH_2 and Rh6G@UIO-66-NH_2 displayed analogous type I isotherms, indicating the existence of abundant micropores and mesopores [33,39]. Moreover, the calculated BET surface area of Rh6G@UIO-66-NH_2 was 292.752 m^2/g, which is considerably smaller than that of pristine UIO-66-NH_2 (461.064 m^2/g). This further confirms the successful synthesis, which is consistent with previous literatures [39,40]. The above results indicated that the microporous channels of the UIO-66-NH_2 support were loaded with Rh6G dyes and may be partly unblocked after encapsulation. These measurements collectively confirm the successful incorporation of Rh6G fluorescein into UiO-66-NH_2 while preserving the skeleton structure and crystalline of UiO-66-NH_2.

3.2. Photophysical properties of Rh6G@UIO-66-NH_2

In order to investigate the influence of Rh6G dye on the optical properties of Rh6G@UiO-66-NH_2 nanocomposites, the 3D front-face fluorescence spectra of UiO-66-NH_2 (Fig. 2A) and Rh6G@UiO-66-NH_2 (Fig. 2B to 2E) were determined. As shown in Fig. 2, UiO-66-NH_2 exhibited a single Excitation/Emission (Ex/Em) peak located at around 370 nm/455 nm, representing the blue emission band attributed to the π-π * transition of the ATA ligand. However, in the fluorescent contour map of Rh6G@UiO-66-NH_2, apart from the MOF peak, another Ex/Em peak at 520 nm/545 nm corresponding to the characteristic fluorescence of Rh6G was also evident. This is noteworthy because in the solid state of Rh6G dye, fluorescence emission is typically absent due to the aggregation-caused quenching (ACQ) phenomenon (Fig. S2). This superior structure of Rh6G@UiO-66-NH_2 inhibits nonradiative energy transfer commonly observed in aggregated dye molecules, thereby preventing quenching of the dye emission [41]. These results further indicate that Rh6G dye molecules were successfully encapsulated without sacrificing their native luminescent properties [42]. Moreover, the synthesized UiO-66-NH_2 powder exhibited a faint yellow color. Visually, the color of Rh6G@UiO-66-NH_2 transitioned from light pink to pink by the naked eye with increasing amount of Rh6G molecules (ranging from 0.5 mM to 2.0 mM). This color change corresponded well with the loading of a greater number of Rh6G dye molecules into the initial UiO-66-NH_2 structure.

According to the 3-D fluorescence spectra of nanocomposites (shown in Fig. 2A-E), drawing a straight line (defined as: Xem = Yex + Δλ, where Δλ = λem - λex) on the 3-D fluorescence spectrum can simulate the result of synchronous fluorescence scanning. The △λ value of synchronous fluorescence can theoretically be predicted from the 3-D fluorescence spectra. In this study, the optimal Δλ condition was set at 60 nm and employed in the following analysis. Both 3-D and synchronous fluorescence spectroscopy can obtain the information on multiple fluorescent substances in the nanocomposites simultaneously. Synchronous fluorescence spectroscopy can simplify spectral analysis by reducing the influence of light scattering and saved detection time, taking only a few seconds for each scan, however 3-D fluorescence spectroscopy needs nearly 5 min for each scanning. As displayed in Fig. S3A, synchronous fluorescence spectra of Rh6G@UiO-66-NH_2 samples with different Rh6G concentrations simultaneously provide information on organic dyes and MOF as well. The Rh6G@UiO-66-NH_2 nanocomposite with 1.0 mM Rh6G exhibited the highest peak intensity at an excitation wavelength near 495 nm among the tested treatments (Fig. S3B). This observation suggests that the appropriate amounts of dye molecules can be accommodated, and Rh6G molecules are gradually isolated within the cages of UiO-66-NH_2, maintaining a monodisperse state. Consequently, concentration-dependent fluorescence enhancement is observed. However, this status was disrupted when the amount of Rh6G dyes exceeded 1.0 mM. Obviously, luminescence quenching occurs, possibly due to non-radiative pathways resulting from the short-range interactions among organic dye molecules. This leads to the occurrence of the ACQ effect within the MOF cages once again [43]. Consequently, a concentration of 1.0 mM Rh6G@UiO-66-NH_2 was chosen to investigate its sensing performance for optimal ratiometric detection of NO_2^-. This concentration was selected because it provides an abundance of active sites while simultaneously safeguarding Rh6G against potential ACQ, making it suitable for subsequent experiments.

As depicted in Fig. 2F, the UV–vis diffuse reflectance spectrum of the Rh6G@UiO-66-NH_2 solid exhibited two distinctive absorption peaks. On the one hand, there was a prominent absorption band ranging from 300 nm to 455 nm, with an absorption peak at 378 nm, attributed to UiO-66-NH_2. This was confirmed by the UV–vis spectrum indicated by

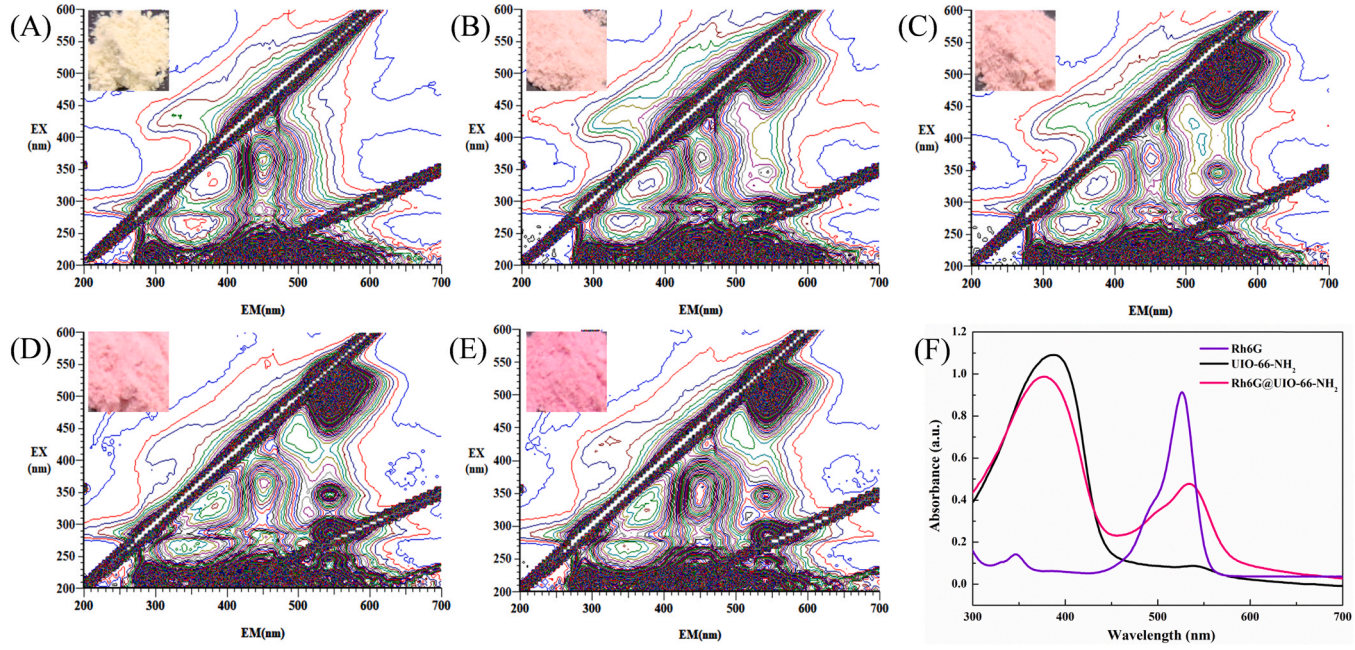

Fig. 2. The 3D-fluorescence spectra of Rh6G@UiO-66-NH_2 solid powders with (A) 0 mM Rh6G, (B) 0.5 mM Rh6G, (C) 1.0 mM Rh6G, (D) 1.5 mM Rh6G, and (E) 2.0 mM Rh6G in aqueous solution. Inset shows a photo of the corresponding UiO-66-NH_2 and Rh6G@UiO-66-NH_2 solid powders. (F) UV–vis absorption spectra of Rh6G, UiO-66-NH_2, and Rh6G@UiO-66-NH_2.

the black line, which is associated with the π → π * electronic transition of the aromatic ring. On the other hand, a characteristic absorption peak of Rh6G appeared at 534 nm, within the range of 458–583 nm after adsorption. This demonstrated a noticeable red shift compared to the absorption peak of the Rh6G solution, indicating the confinement effect of the MOF framework. Taken together, the above results confirmed the successful absorption of fluorescein Rh6G onto the as-prepared UiO-66-NH_2 powder.

3.3. Optimization of detection condition

Moreover, key experimental parameters, containing acidity and reaction time, were optimized for the Rh6G@UiO-66-NH_2 sensing system to achieve the optimal signal response. It can be seen in Fig. 3A that the concentration of HCl in the nanoprobe suspension was varied from 0.01 M to 1.0 M. The fluorescence intensities of both peak MOF (Ex wavelength at 378 nm) and Rh6G (Ex wavelength at 495 nm) reached their maximum values when the HCl concentration was set at 0.05 M. This phenomenon can be attributed to the fact that the rhodamine derivative exhibits a xanthene structure with strong fluorescence emission in such an appropriate acid medium [44]. However, when the HCl concentration exceeded 0.05 M, the fluorescence intensity of peak UIO-66-NH_2 gradually decreased with increasing acidity. The decline may be attributed to the neutralization of the amino groups of MOFs by hydrogen ions in strong acid media, which play a key role in this sensing system. Therefore, for the sake of experimental convenience, 0.05 M of HCl was chosen as the optimal acid condition for the subsequent studies.

Accordingly, to enhence the efficiency of Rh6G@UiO-66-NH_2 in responding to NO_2^-, the influence of reaction time was also investigated. The relationship between the fluorescence intensity ratio of Rh6G@UiO-66-NH_2 (I_{Rh6G}/I_{MOF}) and response time after adding NO_2^- (100 μM) is displayed in Fig. 3B. The results show that the response value I_{Rh6G}/I_{MOF} initially increased as time passed. The change in I_{Rh6G}/I_{MOF} of the sensing system tended to stabilize after a response time of 15 min, indicating that the reaction efficiently and rapidly reached completion. Thus, 15 min was chosen as the optimal reaction time between Rh6G@UiO-66-NH_2 and NO_2^- for further research.

3.4. Establishment of Rh6G@UIO-66-NH_2-based sensor for nitrite

Normally, conventional single-signal fluorescence sensing is easily affected by external conditions and inefficient in detecting NO_2^- in complex samples or aqueous solutions [42]. To address this limitation, a self-calibrated fluorescence sensing platform based on the dual independent fluorescence emission peaks of dye@MOF for ratiometric detection was employed. This approach reduces interference from the external environment and amplifies signal readouts, enabling more sensitive detection. Under optimized conditions, the dual fluorescence response of the Rh6G@UiO-66-NH_2 sensing system was used to detect a range of NO_2^- concentrations (0–1000 μM) (Fig. 4). As the NO_2^- concentration increased, the fluorescence signal of UiO-66-NH_2 (Ex wavelength at 378 nm) was noticeably quenched, along with a decreasing trend in Rh6G fluorescence at 495 nm (Fig. 4A). Besides, the characteristic emission of UiO-66-NH_2 was more significantly quenched than that of Rh6G when low amounts of NO_2^- were added (0–100 μM). This phenomenon may be attributed to the amino groups of UiO-66-NH_2 exposed on the nanocomposite's surface, which are more readily involved in deamination reactions with NO_2^- in the sensing system at the outset. As a result, UiO-66-NH_2, with strong fluorescence, transforms into non-fluorescent UiO-66 in a dispersed water medium due to the changes in electron density. This result is consistent with previous reports reported by Hao et al. [20], where UIO-66-NH_2 was successfully utilized as a fluorescence turn-off probe for the detection of NO_2^- through diazotization and reduction. Subsequently, with higher additions of NO_2^- (over 100 μM), the fluorescence intensity of Rh6G decreased significantly. In acidic conditions, an electron-deficient nitrosyl cation (NO^+), derived from NO_2^-, interacts with the organic dye Rh6G embedded in the MOF framework, forming a nitroso group derivative. The fluorescence of Rh6G gradually quenches due to the weak electron-donating ability of the nitroso group derivative [44,45].

Fig. 4B demonstrated a strong linear relationship between the fluorescence intensity ratio of the sensor (I_{Rh6G}/I_{MOF}) and low concentrations of NO_2^-, ranging from 1 μM to 100 μM, described by the first-order linear equation $I_{Rh6G}/I_{MOF} = 1.21 + 4.68 \times 10^{-2}\ C_1$ (with a correlation coefficient $R^2 = 0.983$). The limit of detection (LOD) for NO_2^- using Rh6G@UiO-66-NH_2 was calculated to be 0.021 μM, following the formula 3σ/s (where σ represents the standard deviation of blank measurements, and s is the slope of the linear calibration plot). This LOD is significantly lower than the maximum allowable concentration of NO_2^- in meat products [44]. Significantly, as depicted in the insert of Fig. 4A, a distinct change in fluorescence color is observable following the quenching process, enabling the visual detection of NO_2^-.

3.5. Selectivity and Anti-interference performance of Rh6G@UIO-66-NH_2 toward nitrite

To assess the selectivity and anti-interference performance of the Rh6G@UIO-66-NH_2 sensing system toward NO_2^-, the impact of various interfering substances on its fluorescence responses was explored. Then, Rh6G@UIO-66-NH_2 was mixed separately with solutions containing

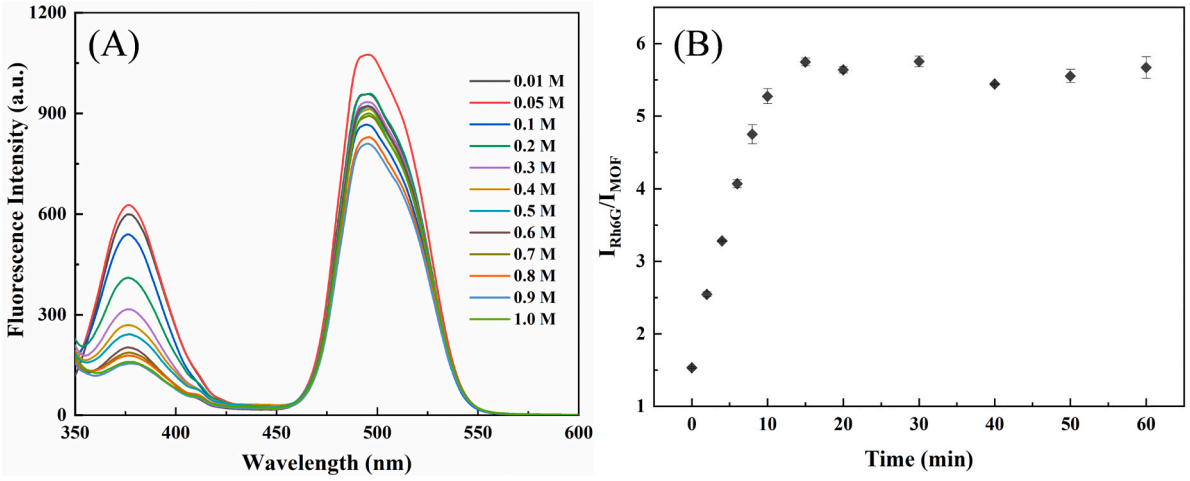

Fig. 3. (A) Effect of HCl concentration (H^+) on fluorescent intensity of Rh6G@UIO-66-NH_2-based sensor. (B) Fluorescence intensity of Rh6G@UIO-66-NH_2 suspension after reaction with nitrite for different times.

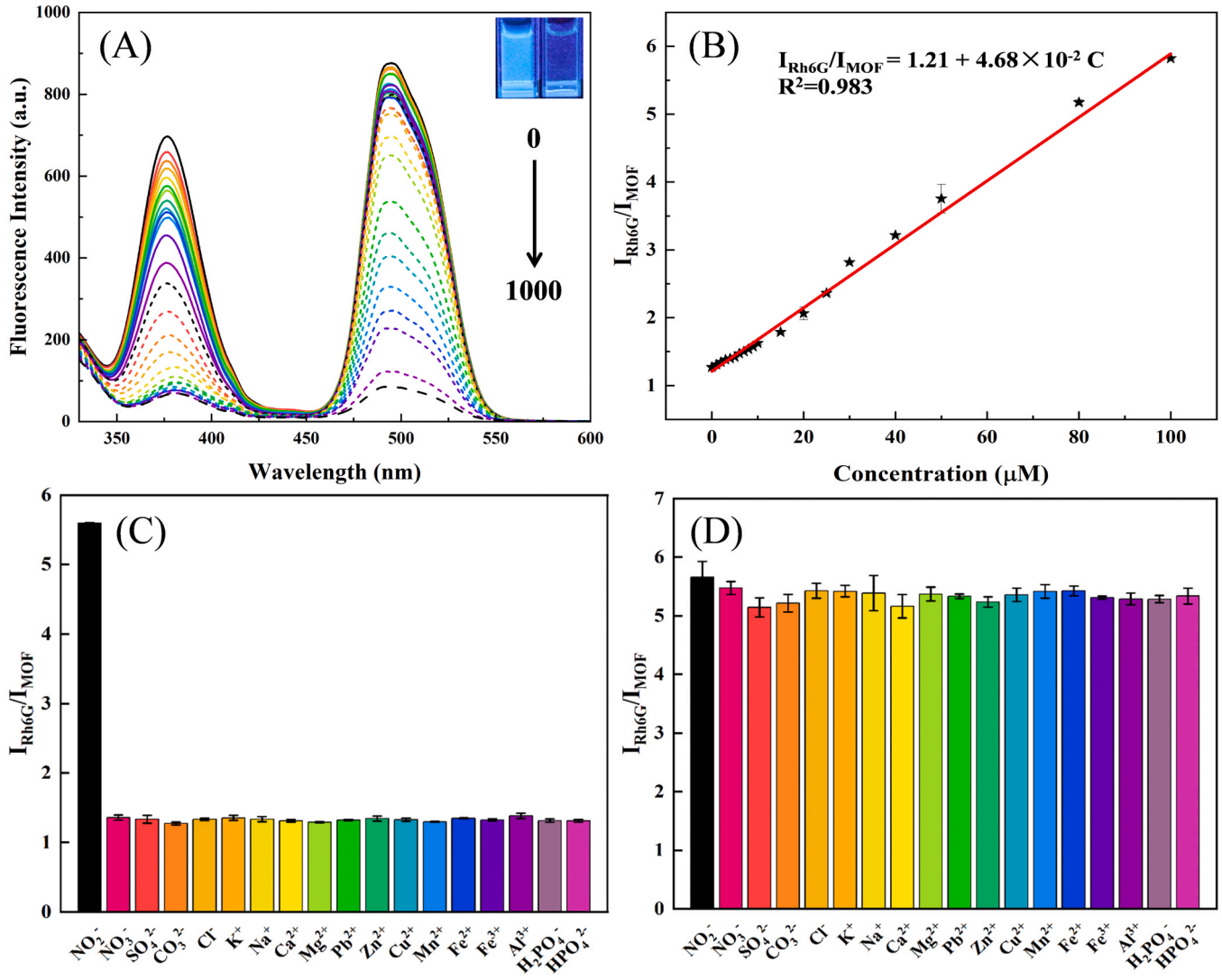

Fig. 4. (A) Synchronous fluorescence spectra of Rh6G@UIO-66-NH_2 suspension toward different concentration of NO_2^- (0–1000 μM). Inset images shows the corresponding photos of Rh6G@UIO-66-NH_2 in the absence (left) and presence (right) of NO_2^- ion under 365 nm UV light. (B) The trends of fluorescent intensity ratio $I_{264\ nm}/I_{440\ nm}$ with different concentration of nitrite. (C) The selectivity and (D) specificity of proposed sensing platform. The concentration of NO_2^- is 100 μM and the concentration of all other interfering substances are ten times higher than NO_2^-.

NO_2^- and other interfering ions, with NO_2^- at a concentration of 100 μM while other interfering substances were fixed at 1 mM. The fluorescent intensity ratio of the nanosensor is displayed in Fig. 4C. In the presence of NO_2^- under 0.05 M HCl, the fluorescence intensity ratio (I_{Rh6G}/I_{MOF}) of Rh6G@UIO-66-NH_2 significantly increased to 5.60. However, treatment with other co-existing interfering ions, including NO_3^-, SO_4^{2-}, CO_3^{2-}, Cl^-, Cr^-, K^+, Na^+, Ca^{2+}, Mg^{2+}, Pb^{2+}, Zn^{2+}, Cu^{2+}, Mn^{2+}, Fe^{2+}, Fe^{3+}, Al^{3+}, $H_2PO_4^-$, and HPO_4^{2-}, had no notable impact on this dual emission nanoprobe. This lack of interference is attributed to the specific interaction between the amino group from Rh6G@UIO-66-NH_2 and NO_2^-. Furthermore, the sensor's resistance to interference is investigated, which is another key criterion for evaluating its performance in practical applications. To evaluate the anti-interference performance, the above-mentioned interfering ions were added to the Rh6G@UIO-66-NH_2 sensing systems designed for NO_2^- detection, thereby conducting a competition experiment. As shown in Fig. 4D, all groups exhibited a distinct enhancement in the fluorescence intensity ratio. This indicates that the influence of these interferents on the NO_2^- detection using the Rh6G@UIO-66-NH_2 detecting platform can be considered negligible. In summary, the above consequences demonstrate that the fabricated nanocomposite meets the sensitivity and selectivity requirements for monitoring NO_2^- in meat products. Furthermore, the facile and efficient preparation procedure introduces innovative concepts for developing new nanosensors.

3.6. Application in real samples

To further verify the practicability and feasibility of the ratiometric fluorescence nanoprobe for the real sample detection, the proposed method based on the Rh6G@UIO-66-NH_2 was applied to determine NO_2^- contents in five commercially available meat samples. The recovery rate was calculated by the standard addition method, and the results are listed in Table S2. The detected NO_2^- concentration in sausage, bacon, ham, stewed beef, and braised chicken were found to be 2.86 mg/kg, 2.43 mg/kg, 3.43 mg/kg, 4.53 mg/kg, and 3.25 mg/kg, respectively. Subsequently, the NO_2^- standard solution was introduced to the samples and analyzed them. The recovery tests yielded results in the range of 94.72%– 104.52%, with relative standard deviations (RSDs) of less than 4%. These outcomes demonstrate the excellent analytical accuracy, precision, and reliability of the designed probe for detecting NO_2^- in meat products. Therefore, the proposed Rh6G@UIO-66-NH_2 nanoprobe holds significant potential as a valuable and efficient novel tool for rapid

NO_2^- detection in practical applications and food safety assessment.

3.7. Precise sensing of nitrite by a portable test Kit

To broaden the practical application of Rh6G@UIO-66-NH_2, it is convenient to develop a portable hydrogel test kit that can be used for on-site screening of NO_2^- to ensure food security and monitor environmental pollution. Gelatin (Gel), derived from the partial hydrolysis of collagen in animal bones and leathers, is an amphoteric biopolymer known for its admirable properties, including good biocompatibility, biodegradability, and nontoxicity [46]. Gelatin itself possesses abundant hydroxyl, amino, and carboxyl functional groups, which make gelation and functionalization easy, facilitating direct chemical reactions between Gel and dye@MOF without the need for additional polymers to form a stable hydrogel compound [47,48]. Hence, Gelatin is selected as a suitable carrier for fabricating a stimuli-responsive hydrogel test kit in this work. The Gel/Rh6G@UIO-66-NH_2 hydrogel compounds were constructed by immobilizing Rh6G@UIO-66-NH_2 into Gel hydrogel, and a commercial microplate was manufactured to create Gel/Rh6G@UIO-66-NH_2 hydrogel arrays, which could serve as a sensing platform for the visualized and fluorometric detection of NO_2^-. Subsequently, to meet the need of on-site analysis, a visual NO_2^- detection method was developed by integrating the Gel/Rh6G@UIO-66-NH_2 hydrogel test kit with a smartphone. This was made possible by leveraging the powerful capabilities of the smartphone's digital camera program and its computational capabilities.

For precise sensing of NO_2^-, the essential 0.05 M HCl was first introduced to various concentrations of NO_2^-, then dropped above cocktail solution of HCl and NO_2^- onto the Gel/Rh6G@UIO-66-NH_2 hydrogel test kit (the detailed experimental procedure is depicted in Scheme 1B). As revealed in Fig. 5A, the colors of the as-prepared hydrogel matrices varied depending on the NO_2^- ion concentrations. Their visible colors changed from pale yellow to golden yellow, and their fluorescence colors changed from bright to dark in a distinct gradient as the NO_2^- concentration increased. Such color-gradient changes are consistent with the results obtained from the Rh6G@UiO-66-NH_2 suspension in the presence of NO_2^- at different concentration, reflecting that gelatin hydrogel does not affect the reaction of NO_2^- with amino group of the Rh6G@UiO-66-NH_2 nanoprobe. After the colorimetric reaction, images of the kit were captured using the built-in cameras of smartphones to identify the visualized and fluorescence color response of Gel/Rh6G@UIO-66-NH_2 hydrogels (Scheme 1B). Through an image processing program, optical image information was directly translated into tonal parameters to realize quantitative NO_2^- detection. As displayed in Fig. 5B, the normalized hue intensity of the kit gradually decreased with increasing NO_2^- concentration (the working concentration of the NO_2^- ions was between 0.1 and 3 mM). A good linear relationship between normalized hue intensity and the concentration of NO_2^- was observed in the range from 0.1 mM to 1.5 mM for the Gel/Rh6G@UIO-66-NH_2 hydrogel test kit under sunlight. The regression equation can be expressed as $y = -0.39\ C + 0.98$ ($R^2 = 0.979$), and the detection limit is calculated to be 0.09 mM (Fig. 5C). Similar results were also obtained in Fig. S4, demonstrating that the normalized hue intensity of the fluorescence color of the test kit exhibited a good linear response ($R^2 = 0.972$) to the NO_2^- concentration in the range of 0.1–1.5 mM. Compared with other previously reported strategies for the detection of NO_2^-, the performance of the detectors based on the Rh6G@UiO-66-NH_2 nanoprobe or Gel/Rh6G@UIO-66-NH_2 hydrogel demonstrated improved selectivity, detection range, and LOD (Table S3).

In addition, selective identification and anti-interference performance are meaningful indices to estimate the practicality of the hydrogel test kit toward the target. Therefore, the afore-mentioned interfering substances were introduced into the hydrogel test kit to simulate practical conditions. Fig. 5D depicts the color change upon adding NO_2^- or common interfering substances into the Gel/Rh6G@UIO-66-NH_2 hydrogels test kit. Only NO_2^- group caused a remarkable response, leading to a noticeable deepening in visible color and a reduction in fluorescence color. The interferences had little effect on the color change of the constructed system, indicating the adequate specificity of the proposed hydrogel kit for NO_2^-. Following, distinct color variations were observed with the naked eye when incubating NO_2^- and co-existing interfering substances together (Fig. 5E). By analyzing the color information (Fig. 5F and G), the normalized intensity histogram further demonstrated that the intensity of the Gel/Rh6G@UIO-66-NH_2 hydrogel test kit was barely affected by interfering substances, whether under sunlight or UV light. Meanwhile, the kit's response to NO_2^- remained constant in the presence of common interferences, revealing excellent specificity and a strong anti-interference capacity. Apart from the excellent specific identification capability of Rh6G@UIO-66-NH_2 toward NO_2^-, another factor contributing to this specificity might be the ability of the Gel hydrogel to act as a barrier, preventing the infiltration of biomacromolecules and small molecules through its porous structure [49]. In summary, the Gel hydrogel, pretreated with Rh6G@UIO-66-NH_2, can be used for on-site monitoring and semi-quantitative analysis of NO_2^- with the naked eye.

4. Conclusions

In conclusion, a ratiometric fluorescence sensing probe (Rh6G@UIO-66-NH_2) for NO_2^- detection in meat products was successfully developed. After combining Rh6G and UIO-66-NH_2, the resulting Rh6G@UIO-66-NH_2 showed significantly improved NO_2^- capture efficiency, along with fast response kinetics, high sensitivity, excellent selectivity, and a low detection limit. The proposed method was successfully applied to detect NO_2^- in five different meat products with a high level of accuracy, indicating its potential for practical applications. Furthermore, a dual-mode portable test kit (Gel/Rh6G@UIO-66-NH_2 hydrogel kit) was further constructed using gelatin hydrogel as a matrix, which was employed for on-site detection of NO_2^- via combining with a smartphone based on fluorescent and visible nanocolorimetry. Owing to its excellent portability, cost-effectiveness, simplicity of operation, rapid response features, and vibrant color display, the Gel/Rh6G@UIO-66-NH_2 hydrogels kit holds great promise and potential for convenient on-site visual detection and precise monitoring of NO_2^- in food samples.

CRediT authorship contribution statement

Siyang Deng: Methodology, Software, Validation, Data curation, Formal analysis, Investigation, Writing – original draft. **Junmei Liu**: Methodology. **Dong Han**: Funding acquisition. **Xinting Yang**: Investigation. **Huan Liu**: Formal analysis, Investigation, Writing – review & editing. **Chunhui Zhang**: Supervision, Project administration, Funding acquisition. **Christophe Blecker**: Supervision, Writing – review & editing.

Environmental Implication

Nitrite (NO_2^-), the most common nitrogen-containing compound in nature, is widely present in the human environment so that it serves as an important indicator of inflammation, food safety, and water quality. Nitrite is widely used in meat products as a color preservative and preservative, however, high levels of nitrites in the diet can be harmful to human health and are associated with the development of certain chronic diseases and cancers. Nitrite should be considered "hazardous material". This study aimed to offers a prospective method for the on-site reliable monitoring and detecting nitrite in food safety and environmental concerns.

Declaration of Competing Interest

The authors declare that they have no known competing financial

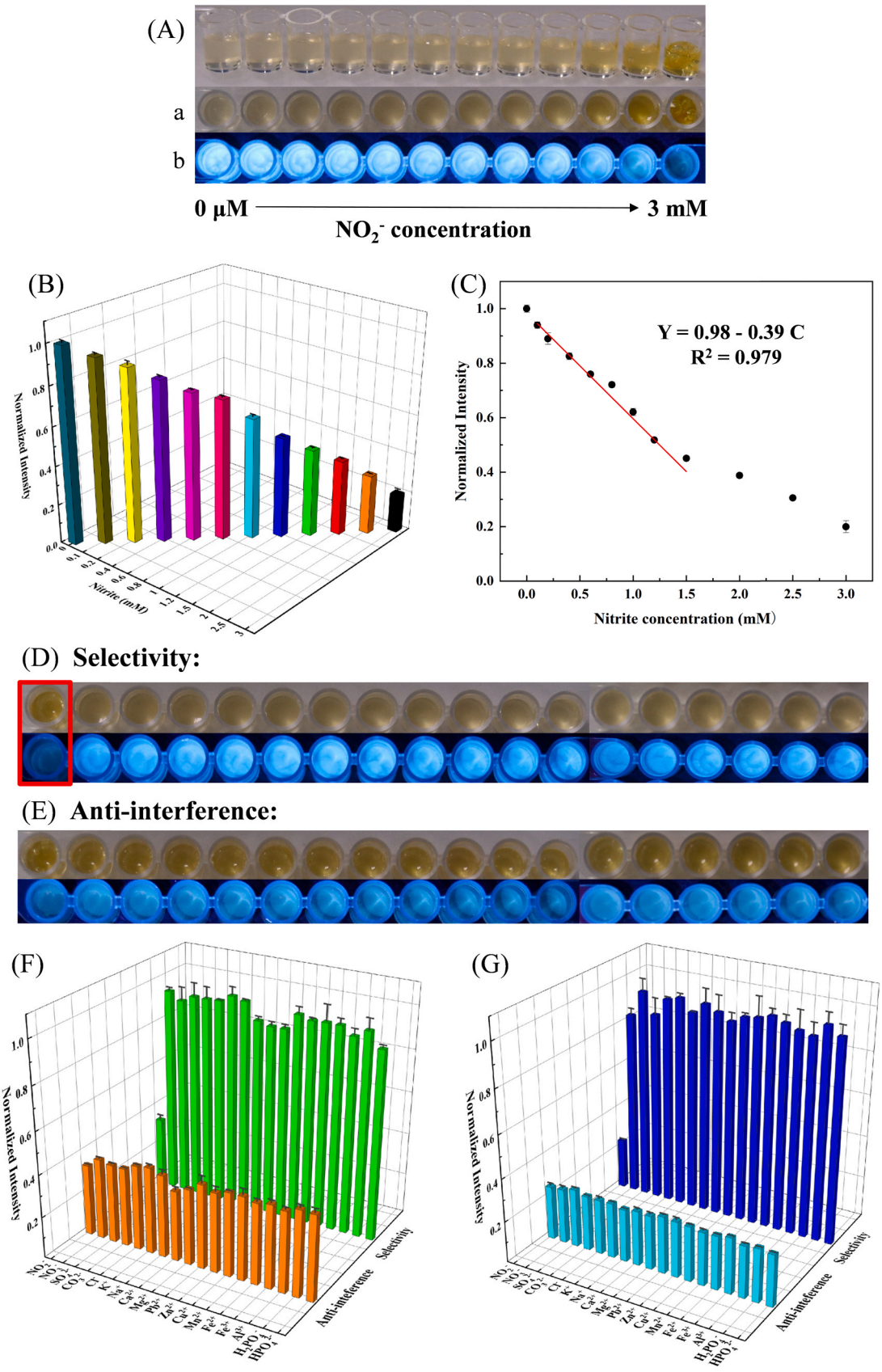

Fig. 5. (A) The photograph of kit with different concentrations of NO_2 under sunlight (a) and UV light (b). (B) The normalized hue intensity of kit digitized by ImageJ software (under sunlight). (C) Corresponding relationship between the concentration of NO_2 and hue intensity (under sunlight). The photographs of kit in the presence of interfering ions, (D): selectivity; (E): anti-interfering. The corresponding normalized hue intensity of selectivity and interference effect in the kit under sunlight (F) and UV light (G).

interests or personal relationships that could have appeared to influence the work reported in this paper.

Data Availability

No data was used for the research described in the article.

Acknowledgement

This project was supported by a research grant from the National Key R & D Program of China (2021YFD2100103), Beijing Science and Technology Planning Project (grant no. Z221100007122010). Siyang Deng's scholarship was sponsored by the China Scholarship Council (CSC).

Appendix A. Supporting information

Supplementary data associated with this article can be found in the online version at doi:10.1016/j.jhazmat.2023.132898.

References

[1] Ledezma-Zamora, K., Sánchez-Gutiérrez, R., Ramírez-Leiva, A., Mena-Rivera, L., 2021. Residual nitrite in processed meat products in Costa Rica: Method validation, long-term survey and intake estimations. Food Chem 361, 130082. https://doi.org/10.1016/j.foodchem.2021.130082.

[2] Hou, C.-Y., Fu, L.-M., Ju, W.-J., Wu, P.-Y., 2020. Microfluidic colorimetric system for nitrite detection in foods. Chem. Eng. J. 398, 125573. https://doi.org/10.1016/j.cej.2020.125573.

[3] Lee, J.H., Alford, L., Kannan, G., Kouakou, B., 2017. Curing properties of sodium nitrite in restructured goat meat (chevon) jerky. Int. J. Food Prop. 20, 526–537. https://doi.org/10.1080/10942912.2016.1168833.

[4] Yang, X., Zhang, M., Xu, J., Wen, S., Zhang, Y., Zhang, J., 2021. Synthesis of fluorescent terbium-based metal-organic framework for quantitative detection of nitrite and ferric ions in water samples. Spectrochim. Acta. A. Mol. Biomol. Spectrosc. 253, 119553 https://doi.org/10.1016/j.saa.2021.119553.

[5] Hospital, X.F., Hierro, E., Stringer, S., Fernández, M., 2016. A study on the toxigenesis by Clostridium botulinum in nitrate and nitrite-reduced dry fermented sausages. Int. J. Food Microbiol. 218, 66–70. https://doi.org/10.1016/j.ijfoodmicro.2015.11.009.

[6] Berardo, A., De Maere, H., Stavropoulou, D.A., Rysman, T., Leroy, F., De Smet, S., 2016. Effect of sodium ascorbate and sodium nitrite on protein and lipid oxidation in dry fermented sausages. Meat Sci 121, 359–364. https://doi.org/10.1016/j.meatsci.2016.07.003.

[7] Skibsted, L.H., 2011. Nitric oxide and quality and safety of muscle based foods. Nitric Oxide 24, 176–183. https://doi.org/10.1016/j.niox.2011.03.307.

[8] Waga, M., Takeda, S., Sakata, R., 2017. Effect of nitrate on residual nitrite decomposition rate in cooked cured pork. Meat Sci 129, 135–139. https://doi.org/10.1016/j.meatsci.2017.03.002.

[9] Rong, M., Wang, D., Li, Y., Zhang, Y., Huang, H., Liu, R., et al., 2021. Green-Emitting Carbon Dots as Fluorescent Probe for Nitrite Detection. J. Anal. Test. 5, 51–59. https://doi.org/10.1007/s41664-021-00161-4.

[10] Berardi, G., Albenzio, M., Marino, R., D'Amore, T., Di Taranto, A., Vita, V., et al., 2021. Different use of nitrite and nitrate in meats: A survey on typical and commercial Italian products as a contribution to risk assessment. LWT 150, 112004. https://doi.org/10.1016/j.lwt.2021.112004.

[11] Deng, S., Bai, X., Li, Y., Wang, B., Kong, B., Liu, Q., et al., 2021. Changes in moisture, colour, residual nitrites and N-nitrosamine accumulation of bacon induced by nitrite levels and dry-frying temperatures. Meat Sci 181, 108604. https://doi.org/10.1016/j.meatsci.2021.108604.

[12] Iammarino, M., Mangiacotti, M., Chiaravalle, A.E., 2020. Anion exchange polymeric sorbent coupled to high-performance liquid chromatography with UV diode array detection for the determination of ten N-nitrosamines in meat products: a validated approach. Int. J. Food Sci. Technol. 55, 1097–1109. https://doi.org/10.1111/ijfs.14410.

[13] Yu, M., Zhang, H., Liu, Y., Zhang, Y., Shang, M., Wang, L., et al., 2022. A colorimetric and fluorescent dual-readout probe based on red emission carbon dots for nitrite detection in meat products. Food Chem 374, 131768. https://doi.org/10.1016/j.foodchem.2021.131768.

[14] Li, S., Qu, J., Wang, Y., Qu, J., Wang, H., 2016. A novel electrochemical sensor based on carbon nanoparticle composite films for the determination of nitrite and hydrogen peroxide. Anal. Methods. 8, 4204–4210. https://doi.org/10.1039/C6AY00030D.

[15] Mako, T.L., Levenson, A.M., Levine, M., 2020. Ultrasensitive Detection of Nitrite through Implementation of N-(1-Naphthyl)ethylenediamine-Grafted Cellulose into a Paper-Based Device. ACS Sens 5, 1207–1215. https://doi.org/10.1021/acssensors.0c00291.

[16] Wang, Q.-H., Yu, L.-J., Liu, Y., Lin, L., Lu, R., Zhu, J., et al., 2017. Methods for the detection and determination of nitrite and nitrate: A review. Talanta 165, 709–720. https://doi.org/10.1016/j.talanta.2016.12.044.

[17] Wu, J.-X., Yan, B., 2018. Luminescent Hybrid Tb^{3+} Functionalized Metal–Organic Frameworks Act as Food Preservative Sensor and Water Scavenger for NO_2^-. Ind. Eng. Chem. Res. 57, 7105–7111. https://doi.org/10.1021/acs.iecr.8b00762.

[18] Zhang, N., Zhang, D., Zhao, J., Xia, Z., 2019. Fabrication of a dual-emitting dye-encapsulated metal–organic framework as a stable fluorescent sensor for metal ion detection. Dalton Trans 48, 6794–6799. https://doi.org/10.1039/C9DT01125K.

[19] Zhang, Y., Gutiérrez, M., Chaudhari, A.K., Tan, J.-C., 2020. Dye-Encapsulated Zeolitic Imidazolate Framework (ZIF-71) for Fluorochromic Sensing of Pressure, Temperature, and Volatile Solvents. ACS Appl. Mater. Interfaces. 12, 37477–37488. https://doi.org/10.1021/acsami.0c10257.

[20] Hao, X., Liang, Y., Zhen, H., Sun, X., Liu, X., Li, M., et al., 2020. Fast and sensitive fluorescent detection of nitrite based on an amino-functionalized MOFs of UiO-66-NH_2. J. Solid State Chem. 287, 121323 https://doi.org/10.1016/j.jssc.2020.121323.

[21] Huang, C., Ye, Y., Zhao, L., Li, Y., Gu, J., 2019. One-Pot Trapping Luminescent Rhodamine 110 into the Cage of MOF-801 for Nitrite Detection in Aqueous Solution. J. Inorg. Organomet. Polym. Mater. 29, 1476–1484. https://doi.org/10.1007/s10904-019-01111-5.

[22] Genis, D.O., Bilge, G., Sezer, B., Durna, S., Boyaci, I.H., 2019. Identification of cow, buffalo, goat and ewe milk species in fermented dairy products using synchronous fluorescence spectroscopy. Food Chem 284, 60–66. https://doi.org/10.1016/j.foodchem.2019.01.093.

[23] Samokhvalov, A., 2020. Analysis of various solid samples by synchronous fluorescence spectroscopy and related methods: A review. Talanta 216, 120944. https://doi.org/10.1016/j.talanta.2020.120944.

[24] Włodarska, K., Khmelinskii, I., Sikorska, E., 2018. Authentication of apple juice categories based on multivariate analysis of the synchronous fluorescence spectra. Food Control 86, 42–49. https://doi.org/10.1016/j.foodcont.2017.11.004.

[25] Dankowska, A., Kowalewski, W., 2019. Comparison of different classification methods for analyzing fluorescence spectra to characterize type and freshness of olive oils. Eur. Food Res. Technol. 245, 745–752. https://doi.org/10.1007/s00217-018-3196-z.

[26] Lu, Z., Wu, M., Wu, S., Yang, S., Li, Y., Liu, X., et al., 2016. Modulating the optical properties of the AIE fluophor confined within UiO-66's nanochannels for chemical sensing. Nanoscale 8, 17489–17495. https://doi.org/10.1039/C6NR05600H.

[27] Ma, X., Chai, Y., Li, P., Wang, B., 2019. Metal–Organic Framework Films and Their Potential Applications in Environmental Pollution Control. Acc. Chem. Res. 52, 1461–1470. https://doi.org/10.1021/acs.accounts.9b00113.

[28] Badsha, M.A.H., Khan, M., Wu, B., Kumar, A., Lo, I.M.C., 2021. Role of surface functional groups of hydrogels in metal adsorption: From performance to mechanism. J. Hazard. Mater. 408, 124463 https://doi.org/10.1016/j.jhazmat.2020.124463.

[29] Javanbakht, S., Hemmati, A., Namazi, H., Heydari, A., 2020. Carboxymethylcellulose-coated 5-fluorouracil@MOF-5 nano-hybrid as a bio-nanocomposite carrier for the anticancer oral delivery. Int. J. Biol. Macromol. 155, 876–882. https://doi.org/10.1016/j.ijbiomac.2019.12.007.

[30] Wang, L., Xu, H., Gao, J., Yao, J., Zhang, Q., 2019. Recent progress in metal-organic frameworks-based hydrogels and aerogels and their applications. Coord. Chem. Rev. 398, 213016 https://doi.org/10.1016/j.ccr.2019.213016.

[31] Hou, L., Qin, Y., Li, J., Qin, S., Huang, Y., Lin, T., et al., 2019. A ratiometric multicolor fluorescence biosensor for visual detection of alkaline phosphatase activity via a smartphone. Biosens. Bioelectron. 143, 111605 https://doi.org/10.1016/j.bios.2019.111605.

[32] Katz, M.J., Brown, Z.J., Colón, Y.J., Siu, P.W., Scheidt, K.A., Snurr, R.Q., et al., 2013. A facile synthesis of UiO-66, UiO-67 and their derivatives. Chem. Commun. 49, 9449 https://doi.org/10.1039/c3cc46105j.

[33] Shi, J., Chen, F., Hou, L., Li, G., Li, Y., Guan, X., et al., 2021. Eosin Y bidentately bridged on UiO-66-NH_2 by solvothermal treatment towards enhanced visible-light-driven photocatalytic H_2 production. Appl. Catal. B Environ. 280, 119385 https://doi.org/10.1016/j.apcatb.2020.119385.

[34] Deng, S., Liu, H., Zhang, C., Yang, X., Blecker, C., 2022. LMOF serve as food preservative nanosensor for sensitive detection of nitrite in meat products. LWT 169, 114030. https://doi.org/10.1016/j.lwt.2022.114030.

[35] Aghili, F., Ghoreyshi, A.A., Rahimpour, A., Van der Bruggen, B., 2020. New Chemistry for Mixed Matrix Membranes: Growth of Continuous Multilayer UiO-66-NH_2 on UiO-66-NH_2-Based Polyacrylonitrile for Highly Efficient Separations. Ind. Eng. Chem. Res. 59, 7825–7838. https://doi.org/10.1021/acs.iecr.9b07063.

[36] Aghili, F., Ghoreyshi, A.A., Van der Bruggen, B., Rahimpour, A., 2021. Introducing gel-based UiO-66-NH_2 into polyamide matrix for preparation of new super hydrophilic membrane with superior performance in dyeing wastewater treatment. J. Environ. Chem. Eng. 9, 105484 https://doi.org/10.1016/j.jece.2021.105484.

[37] Cao, M., Xiao, F., Yang, Z., Chen, Y., Lin, L., 2022. Purification of oil-containing emulsified wastewater via PAN nanofiber membrane loading PVP-UiO-66-NH_2. Sep. Purif. Technol. 297, 121514 https://doi.org/10.1016/j.seppur.2022.121514.

[38] Gao, N., Huang, J., Wang, L., Feng, J., Huang, P., Wu, F., 2018. Ratiometric fluorescence detection of phosphate in human serum with a metal-organic frameworks-based nanocomposite and its immobilized agarose hydrogels. Appl. Surf. Sci. 459, 686–692. https://doi.org/10.1016/j.apsusc.2018.08.092.

[39] Jiao, C., Hu, M., Hu, T., Zhang, J., 2023. Enhanced proton conductivity and overall water splitting efficiency of dye@MOF by post-modification of MOF. J. Solid State Chem. 322, 123978 https://doi.org/10.1016/j.jssc.2023.123978.

[40] Li, W., Liu, Z., Wang, L., Gao, G., Xu, H., Huang, W., et al., 2023. FeSx@MOF-808 composite for efficient As(III) removal from wastewater: behavior and mechanism. J. Hazard. Mater. 446, 130681 https://doi.org/10.1016/j.jhazmat.2022.130681.
[41] Guo, L., Liu, Y., Kong, R., Chen, G., Liu, Z., Qu, F., et al., 2019. A Metal–Organic Framework as Selectivity Regulator for Fe^{3+} and Ascorbic Acid Detection. Anal. Chem. https://doi.org/10.1021/acs.analchem.9b03143.
[42] Yoo, J., Ryu, U., Kwon, W., Choi, K.M., 2019. A multi-dye containing MOF for the ratiometric detection and simultaneous removal of $Cr_2O_7^{2-}$ in the presence of interfering ions. Sens. Actuators B Chem. 283, 426–433. https://doi.org/10.1016/j.snb.2018.12.031.
[43] Ye, Y., Zhao, L., Hu, S., Liang, A., Li, Y., Zhuang, Q., et al., 2019. Specific detection of hypochlorite based on the size-selective effect of luminophore integrated MOF-801 synthesized by a one-pot strategy. Dalton Trans 48, 2617–2625. https://doi.org/10.1039/C8DT04692A.
[44] Zhang, Y., Su, Z., Li, B., Zhang, L., Fan, D., Ma, H., 2016. A Recyclable Magnetic Mesoporous Nanocomposite with Improved Sensing Performance toward Nitrite. ACS Appl. Mater. Interfaces. 8, 12344–12351. https://doi.org/10.1021/acsami.6b02133.
[45] Viboonratanasri, D., Pabchanda, S., Prompinit, P., 2018. Rapid and simple preparation of rhodamine 6G loaded HY zeolite for highly selective nitrite detection. Appl. Surf. Sci. 440, 1261–1268. https://doi.org/10.1016/j.apsusc.2018.01.156.
[46] Abou-Zeid, R.E., Awwad, N.S., Nabil, S., Salama, A., Youssef, M.A., 2019. Oxidized alginate/gelatin decorated silver nanoparticles as new nanocomposite for dye adsorption. Int. J. Biol. Macromol. 141, 1280–1286. https://doi.org/10.1016/j.ijbiomac.2019.09.076.
[47] Njaramba, L.K., Kim, M., Yea, Y., Yoon, Y., Park, C.M., 2023. Efficient adsorption of naproxen and ibuprofen by gelatin/zirconium-based metal–organic framework/sepiolite aerogels via synergistic mechanisms. Chem. Eng. J. 452, 139426 https://doi.org/10.1016/j.cej.2022.139426.
[48] Yang, W., Wang, J., Han, Y., Luo, X., Tang, W., Yue, T., et al., 2021. Robust MOF film of self-rearranged UiO-66-NO_2 anchored on gelatin hydrogel via simple thermal-treatment for efficient Pb(II) removal in water and apple juice. Food Control 130, 108409. https://doi.org/10.1016/j.foodcont.2021.108409.
[49] Wang, T., Zhang, L., Xin, H., 2022. A Portable Fluorescent Hydrogel-Based Device for On-Site Quantitation of Organophosphorus Pesticides as Low as the Sub-ppb Level. Front. Chem. 10. https://www.frontiersin.org/articles/10.3389/fchem.2022.855281.